North Pacific Subtropical Mode Water Volume and Density Anomalous Decrease in a Recent Stable Kuroshio Extension Period from Argo Observations

Jing Sheng[1], Cong Liu[2], Yanzhen Gu[1], Peiliang Li[1,2], Fangguo Zhai[3], Ning Zhou[1,2]

[1]Ocean College, Zhejiang University, Zhoushan, 316000, China
[2]Hainan Institute of Zhejiang University, Sanya, 572000, China.
[3]College of Oceanic and Atmospheric Science, Ocean University of China, Qingdao, 266000, China.

Correspondence to: Cong Liu (liucong175@gmail.com)

Abstract. North Pacific subtropical mode water (NPSTMW) is formed as the low stratification water mass in the wintertime mixed layer south of the Kuroshio Extension (KE). In a recent period of 2018-2021, the KE jet is in a persisting stable dynamic state. But based on analysis of Argo observation, the mean volume of NPSTMW in ventilation region drop anomalously by ~21% during 2018-2021 relative to 2012-2015 when the KE jet is likewise stable. Moreover, the NPSTMW volume in denser density range (approximately $\sigma_\theta > 25.2$ kg m^{-3}) starts to decrease but the volume of lighter density of the NPSTMW increases since 2018. The decreasing of the NPSTMW subduction and formation rate are associated with anomalously shallow wintertime mixed layer depth (MLD) and weak heat loss in the NPSTMW formation region. The interannual variations of the NPSTMW subduction and formation reflect the variability of the overlying atmosphere which is correlated with Pacific decadal oscillation (PDO) shift in 2018-2021. When the PDO shifts from its positive to a negative phase in analysis period, the effects of local wind stress anomalies seem to play an evident role in driving the variability of NPSTMW on interannual time scales. The MLD and heat loss change during the cold season in 2018-2021 are strongly coupled with the poleward shift of the westerlies-which cause the weaker wintertime wind and the easterly wind anomalies over the NPSTMW formation region. The declines of heat loss and southward Ekman transport, owing to the wind stress anomalies, further prohibit the upper-ocean convection and mixed layer deepening and cooling. Additionally, the insufficient development of wintertime MLD in 2018-2021 may also be correlated with the significantly intensified preconditioning of near surface stratification (<150 m depth) due to the persisting near surface warming.

1 Introduction

North Pacific Subtropical Mode Water (NPSTMW) is one of the most remarkable low potential vorticity (PV) (i.e., the low stratification) water masses that can be found in the subsurface layer of the western part of the subtropical gyre in the North Pacific Ocean (Oka and Qiu, 2012; Suga et al., 1989). The NPSTMW formation processes are involved in transformation, formation, and subduction of the water mass in upper-ocean (i.e., thermodynamic and dynamic processes, Marshall et al.,

30   1999; Nishikawa et al., 2013). Hence, the mode waters retain the memory of the atmospheric condition at the formation time
and are key to understanding interannual-to-interdecadal climate variability (Wu et al., 2020, 2021). They play an important
role in modulating the ocean ventilation process accompanying biogeochemical variability (Oka et al., 2015, 2019).

NPSTMW are formed in a deep wintertime mixed layer (ML) south of the Kuroshio Extension (KE), controlling the
ventilation process of the upper-ocean, due to the ocean-atmospheric interaction in wintertime (Oka and Qiu, 2012). Many

35   previous observations and numerical experiments have studied the related factors of interannual to decadal variations in
NPSTMW. The early studies have pointed out that the few strong wintertime air-sea heat flux loss events driven by the East
Asian monsoon (e.g., Hanawa & Kamada, 2001; Masuzawa, 1969; Rainville et al., 2007; Suga & Hanawa, 1995; Taneda et
al., 2000) dominate the interannual variations in NPSTMW formation. Davis et al. (2011) then identified the interannual
variability of NPSTMW volume is correlated with the role of the surface heat flux and large-scale wind stress patterns due to

40   the Pacific decadal oscillation (PDO, Newman et al., 2016) shift with a zero-time lag. A negative (positive) PDO index
implies a weaker (stronger) Aleutian low (AL), weaker (stronger) westerlies, and higher (lower) sea surface temperature
(SST) in the western North Pacific subtropical gyre region (Qiu, 2003). A weaker (stronger) wind stress over the NPSTMW
formation region results in less (more) heat loss to the atmosphere and less (more) NPSTMW. In addition, the weaker
westerlies in the NPSTMW formation area produces less Ekman transport of the cold water from north and the resulting

45   warmer subsurface ocean inhabits wintertime convection and deep ML formation. However, Qiu & Chen (2006) attributed
the decadal variability of NPSTMW to the role of the first-mode baroclinic Rossby waves and quasi-decadal variability of
the dynamic state of the KE jet in associated with the PDO. This mechanism has been demonstrated by the successive
studies (e.g., Cerovečki & Giglio, 2016; Oka et al., 2015; Qiu et al., 2007; Sugimoto & Hanawa, 2010; Toyama et al., 2015).
During the positive (negative) PDO phase, namely when the AL is stronger (weaker), while positive (negative) wind stress

50   curl anomalies that are generated give rise to the enhanced Ekman flux divergence, resulting in negative (positive) sea
surface height (SSH) and negative (positive) main thermocline depth (MTD) anomalies in the central North Pacific, and then
propagate westward at the speed of the first-mode baroclinic Rossby waves. When the anomalies reach the area east of Japan
with a time lag of 3-5 years, KE turns into an unstable (stable) state accompanying a high (low) regional eddy activity (Qiu
and Chen, 2005). Especially, during the unstable KE period, more cyclonic eddies are detached from KE to the southern

55   recirculation gyre (Sasaki and Minobe, 2015), supplying the relatively high potential vorticity (PV) water from north of KE
to hinder the formation of deep ML. Anomalous shoaling of the MTD and stronger background stratification in the
NPSTMW formation region, both associated with a negative PDO phase, provide unfavorable oceanic conditions for the
development of deep wintertime ML associated with the NPSTMW (Sugimoto and Hanawa, 2010; Sugimoto and Kako,
2016). (Cerovečki and Giglio, 2016) also demonstrated that the strong NPSTMW density decrease that documented by Argo

60   in 2009 is modulated by a negative density anomaly started to propagated westward from the central Pacific about three
years later when the PDO index switched from positive to negative. Finally, the surface density decrease provided oceanic
preconditioning for preferential surface formation of a lighter variety of NPSTMW. Cerovečki et al. (2019) expand on the
Davis et al. (2011) analysis of the strong NPSTMW volume decrease in 1996-1999, they also found that strong NPSTMW

density decrease played a crucial role in the strong NPSTMW volume decrease in 1999. The near-surface density decrease is caused by temperature increase, in turn caused by an increase in KE geostrophic transport at the time when the KE jet changes from a contracted into an elongated state starting in 1997 (Qiu, 2000). Both processes increased the PV in the NPSTMW region, decreasing the volume of water in the NPSTMW density range. Although locally governed by different physical processes, both NPSTMW volume and density decrease are part of quasi-decadal variability caused by basin-wide changes in wind stress curl.

In recent years, KE is in a stable state associated with the Kuroshio large-meander (LM) path south of Japan (Figure 1). Although a persisting Kuroshio LM and the resultant stable state of the KE has already exceeded four years (Qiu and Chen, 2021; Usui, 2019), the NPSTMW volume has declined since 2018 (Oka et al., 2021). Thus, it is of interest to examine what predominantly determines such variability of NPSTMW (2018-2021). By analyzing in situ observational data, we are about to identify the physical processes governing the persisting decline of NPSTMW in recent years when the KE jet is stable.

Argo observations were used to gain a better understanding of the temporal variability of the NPSTMW, and to identify its associated atmospheric forcing and oceanic forcing. The rest of this paper is structured as follows: Section 2 describes the data, methods and the mean characteristics of NPSTMW defined in this study. Section 3 describes the recent decreases of NPSTMW volume and density corresponding to the subduction and surface formation rate anomalies, respectively. The mechanisms that give rise to interannual variations in the subduction and formation of NPSTMW is further discussed in Section 3. Section 4 contains a summary and concluding remarks.
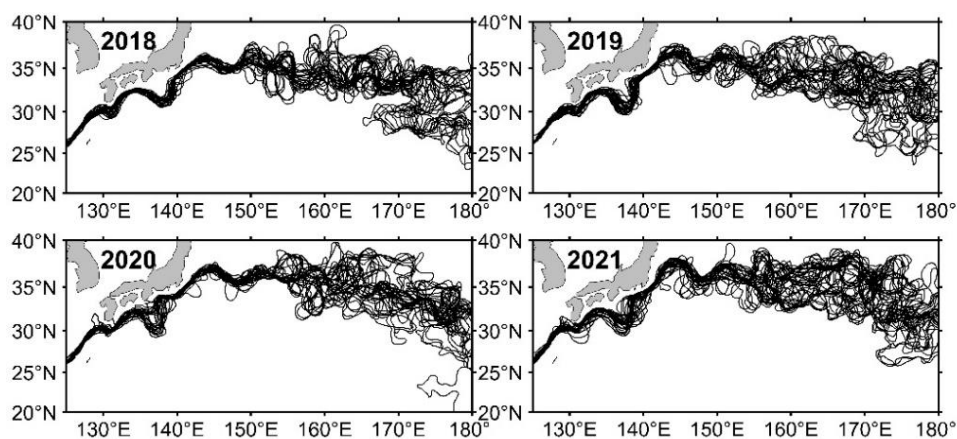
Figure 1: Yearly (in the Kuroshio LM period) paths of the Kuroshio and its extension defined by 110 cm contours in the weekly SSH fields that reconstructed from CMEMS satellite-derived altimetry SSH anomaly data and mean dynamic topography data. Here paths are plotted every 14 days.

2 Data and Processing Procedures

2.1 Data

The formation and distribution of the NPSTMW are briefly located in an area bounded on 20°N-40°N and on 125°E-180° (east of the islands of Japan, Liu et al., 2017). We use the most recent updated gridded Argo product with a horizontal resolution of 1°×1° obtained by Roemmich and Gilson (referred to as the RG dataset below; Roemmich & Gilson, 2009), which includes the Argo-only derived monthly temperature and salinity fields covering the period from 2004 to 2021. In addition, we also use individual Argo profiles, owing to their better vertical resolution than the gridded data, to ensure the recent variability of NPSTMW in the NPSTMW formation region and enable a detailed description of NPSTMW change. The quality-controlled individual Argo profiles are edited according to the procedures of Oka et al. (2007). The profiles almost cover the whole region of the NPSTMW formation and distribution, especially in the zone west of 155°E (Figure 2a). The monthly atmospheric variables of net surface heat flux (HF; the sum of latent heat flux, sensible heat flux, net surface longwave radiation flux, and net shortwave radiation flux), evaporation (E), precipitation (P) and wind stress for periods from 2004 to 2021 are from the ECMWF ERA5 reanalysis with a horizontal resolution of 1/4°×1/4° (Hersbach et al., 2019). The zonal and meridional surface geostrophic velocity anomalies, sea surface height (SSH) anomaly data and mean dynamic topography data are provided by the Copernicus Marine Environment Monitoring Service (CMEMS). The CMEMS dataset derived from satellite altimetry has a one-day temporal resolution and a 1/4° spatial resolution from January 1993 to December 2021.
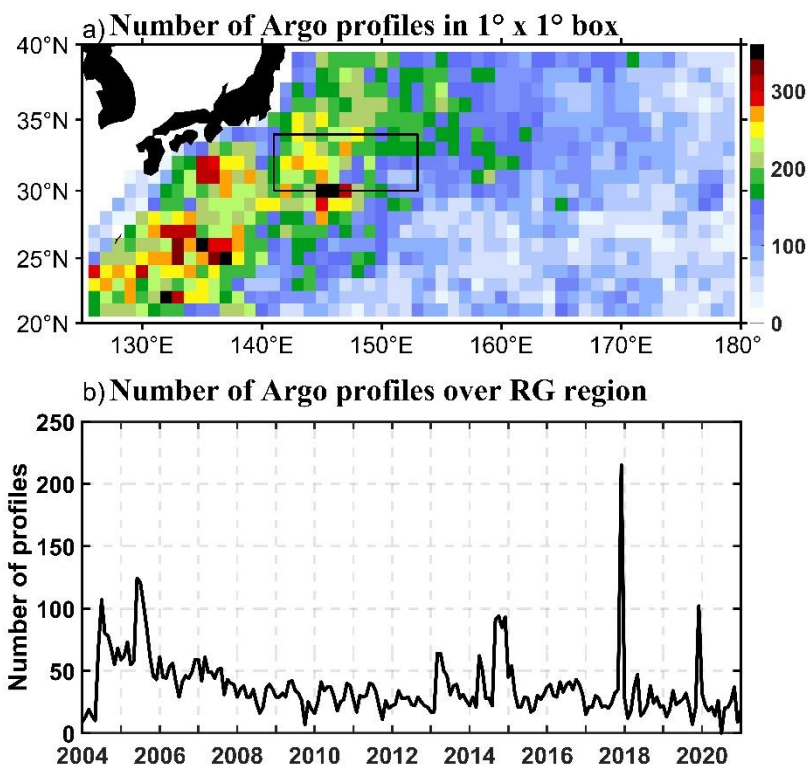
Figure 2: Number of Argo profiles in (a) each $1° \times 1°$ box (black solid box shows the RG region south of KE), and (b) over the entire RG region south of KE (30°N-34°N, 141°E-153°E) for the period from January 2004 to December 2021 (Note that profiles north of the KE are excluded).

2.2 Mean characteristics of the NPSTMW

The NPSTMW is formed in the deep winter ML (Suga and Hanawa, 1990). In this study, NPSTMW is defined as a water mass with a low-PV (PV<2.0×10^{-10} m^{-1} s^{-1}) in the potential density range of σ_θ=25.0-25.5 kg m^{-3} (Figure 3). The potential vorticity is defined as $\mathrm{PV} = -(f / \rho_0)(\partial \sigma_\theta / \partial z)$, where f is the Coriolis parameter, ρ_0 is a reference density (1025 kg m^{-3}), σ_θ is the potential density (Liu et al., 2017). The mixed layer depth (MLD) is defined as the depth at which the potential density is different from the sea surface (10 m) density by 0.125 kg m^{-3} (Levitus, 1982).

The narrow latitudinal extent of the NPSTMW formation extends from 30°N to the KE jet near 35°N (i.e., the upstream KE recirculation gyre; referred to as the RG region below). The part of the NPSTMW then can be advected downstream to the date line and to the subtropical front (Oka and Qiu, 2012; Qiu et al., 2006). Due to focusing on individual profiles detecting NPSTMW formation in the RG region south of the KE (30°N-34°N, 141°E-153°E; Figure 2a), we use only profiles with temperature (T>16°C) at 200 m to minimize the possibility of identifying subarctic profiles coming from north of the KE, according to the procedures of Sugimoto & Kako (2016). Figure 2b displays the number of profiles in which the MLD and

thickness of NPSTMW was detected in the RG region south of KE, revealing that more than 30 profiles are available for most months. Temperature and salinity at each profile are interpolated onto a 1 m vertical grid using the Akima spline

120   (Akima, 1970). We use a 12°C isotherm as an indicator of the MTD in the western part of the North Pacific Subtropical gyre (Uehara et al., 2003).
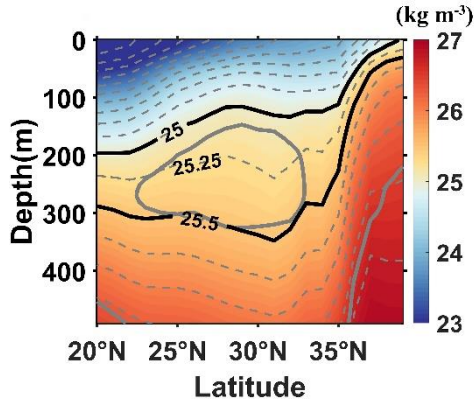
Figure 3: The meridional section at 150°E of climatological annual mean potential density (color shading and thin gray dashed contours with σ_θ =0.25 kg m^{-3} interval) based on the 2004-2021 period averages of the RG dataset. The thick black solid contours

125   **(σ_θ =25.0 kg m^{-3} and σ_θ =25.5 kg m^{-3}) are the isopycnals bounding the density range of NPSTMW, and the thick gray solid contour bounds the low PV pool with PV<2$\times$10^{-10} m^{-1} s^{-1}.**

2.3 Formation and subduction of NPSTMW

The subduction rate is defined as the rate at which the water mass is transferred from the ocean surface layer into the main thermocline. The instantaneous subduction rate ($s(t)$) of water mass that leaves the ML in the Eulerian coordinates is given

130   by (Cushman-Roisin, 1987):

$$s(t) = -\left(\frac{\partial h}{\partial t} + \mathbf{u} \cdot \nabla h + w \right), \tag{1}$$

where h is the mixed layer depth (MLD). The rate of mixed layer shoaling is the temporal induction ($-\frac{\partial h}{\partial t}$). The lateral

induction rate at which the water is swept beneath the shallowing MLD is by horizontal advection ($-\mathbf{u} \cdot \nabla h$), -$w$ refers to

the vertical pumping and ∇ is the horizontal gradient operator. Using the temperature and salinity profiles at each grid point

135   from the RG dataset, we compute the horizontal geostrophic velocity field $\mathbf{u}$ relative to 1000 m with a horizontal resolution

of 1°$\times$1° (Oka et al., 2011). The vertical pumping $w = \text{curl}(\mathbf{\tau}/(\rho_0 f))$ is calculated from wind stress ($\mathbf{\tau}$) provided by the

ERA5, and ρ_0 =1025 kg m^{-3}.

Practically, the formation process of mode water is that the low-PV water mass at the base of late winter mixed layer is subducted into the ocean interior (Oka and Qiu, 2012). Thus, we adapt the low-PV of water subducted at the base of the

140 mixed layer in the ventilation regime, which is expressed as (Williams, 1989, 1991):

$$Q = \frac{f}{\rho_0} \frac{\frac{\partial \rho_{\mathrm{m}}}{\partial t} + \mathbf{u}_{\mathrm{b}} \cdot \nabla \rho_{\mathrm{m}}}{s},$$ (2)

where $\mathbf{u}_{\mathrm{b}}$ is the horizontal velocity at the base of the mixed layer. ρ_{m} and ρ_0 are the mixed layer density and reference density, respectively. s respresents the subduction rate.

Since the instantaneous subduction rate fluctuates considerably, the annual mean subduction rate (s_{ann}) is defined as (Wu et

145 al., 2021):

$$s_{\mathrm{ann}} = \frac{1}{T_0} \int_{T_{\mathrm{s}}^{\mathrm{ef}}}^{T_{\mathrm{e}}^{\mathrm{ef}}} s(t) dt,$$ (3)

where T_0 is one year, $T_{\mathrm{s}}^{\mathrm{ef}}$ and $T_{\mathrm{e}}^{\mathrm{ef}}$ are the times when effective subduction starts and ends, respectively. The effective subduction period is fixed in late winter (February-April, Oka et al., 2015).

Before the effective subduction period in late winter, the fluid passes laterally across outcropping isopycnals at sea surface in

150 winter; the transformation of fluid that makes up a particular density layer is modified either by surface buoyancy flux, vertical diffusion, or eddy buoyancy fluxes (e.g.,Garrett & Tandon, 1997; D. Marshall, 1997; J. Marshall et al., 1999; Walin, 1982). In practice, the water mass transformation at time t is calculated using discrete density intervals but considering the air-sea flux only (neglecting interior mixing, Cerovečki et al., 2019; Cerovečki & Marshall, 2008):

$$T(\sigma_\theta, t) = -\frac{\partial}{\partial \sigma_\theta} \iint_{A_{\sigma_\theta}} B_{\mathrm{surf}} dA,$$ (4)

155 Here, A_{σ_θ} is the surface area of the outcrop window for σ_θ within the density interval $[\sigma_\theta - \Delta\sigma_\theta/2, \sigma_\theta + \Delta\sigma_\theta/2]$ separated by the density increment $\Delta\sigma_\theta$. Transformation has units of Sverdrups (Sv; 1Sv=10^6 m^3 s^{-1}). The surface buoyancy flux (B_{surf}) is given by:

$$B_{\mathrm{surf}} = -\frac{\alpha}{C_p} \mathrm{HF} + \beta\rho_0 S_0 (E - P),$$ (5)

Where α and β are the thermal expansion and saline contraction coefficients, respectively. C_{p} is the specific heat of

160 seawater. S_0 is the sea surface water salinity. ρ_0 is the sea surface density.

The convergence of the air-sea transformation rate in the density interval $[\sigma_\theta - \Delta\sigma_\theta/2, \sigma_\theta + \Delta\sigma_\theta/2]$ yields the air-sea formation rate (Guo et al., 2018; Small et al., 2022):

$$M(\sigma_\theta)\Delta\sigma_\theta = T\left(\sigma_\theta - \frac{\Delta\sigma_\theta}{2}, t\right) - T\left(\sigma_\theta + \frac{\Delta\sigma_\theta}{2}, t\right), \tag{6}$$

Here, M is the water mass accumulation per unit density (i.e., the convergence of water mass transformation in density space)
165 and $M\Delta\sigma_\theta$ is referred to as the water mass formation (with units of Sv).

3 Results

3.1 NPSTMW volume loss and density decrease in 2018-2021

The monthly time series of NPSTMW volume and that binned into potential density at σ_θ=0.05 kg m^{-3} are shown in Figure 4a and 4b. The NPSTMW volume change is modulated by the variability of KE state since 2004 (Oka et al., 2021). Except
170 for a short time of 2006-2009 when the KE jet is unstable, the NPSTMW volume has a dramatic decrease during 2006-2009. The volume of NPSTMW has restored and subsequently increased largely during 2012-2015 when the KE is stable. But in recent stable KE period, it is worthy to note that NPSTMW volume in analysis region gradually decreased since 2018. The mean total volume of NPSTMW drop by ~21% during 2018-2021 on average relative to 2012-2015. Particularly, the NPSTMW volume in denser density range (approximately σ_θ>25.2 kg m^{-3}) since 2018 appears to decrease from 6.13$\times10^{14}$
175 m^3 in 2018 to 4.77 $\times10^{14}$ m^3 in 2021, but the NPSTMW volume in lighter density range (approximately σ_θ<25.2 kg m^{-3}) increases from 1.93$\times10^{14}$ m^3 in 2018 to 2.19$\times10^{14}$ m^3 in 2021. It means the density of NPSTMW has declined accompanied with the NPSTMW volume loss in 2018-2021 (Figure 4a). The averaged maximum NPSTMW thickness in April to May when annual newly NPSTMW formed also started to gradually decrease since 2018. The mean thickness of NPSTMW in April to May from 2018-2021 has approximately dropped by 50 m. There similarly seems to be a persistent loss of newly
180 NPSTMW formation in 2018-2021.

The NPSTMW volume and density increase in 2012-2015 coincided with a period when the KE is in its stable dynamic state. However, what causes the anomalous decline of the NPSTMW during a recent period of stable KE state? Was the observed decrease of newly formed NPSTMW volume and density in 2018-2021 predominantly caused by a decrease in surface formation in the NPSTMW density range and a decrease in subduction of low-PV water in the NPSTMW density range?
185 Furthermore, was the observed decrease of NPSTMW in a recent stable KE period related in some ways to local and distant effects of atmospheric forcing or oceanic precondition, as suggested by Davis et al. (2011) and Sugimoto & Hanawa (2010)? We address these questions in the subsequent sections.
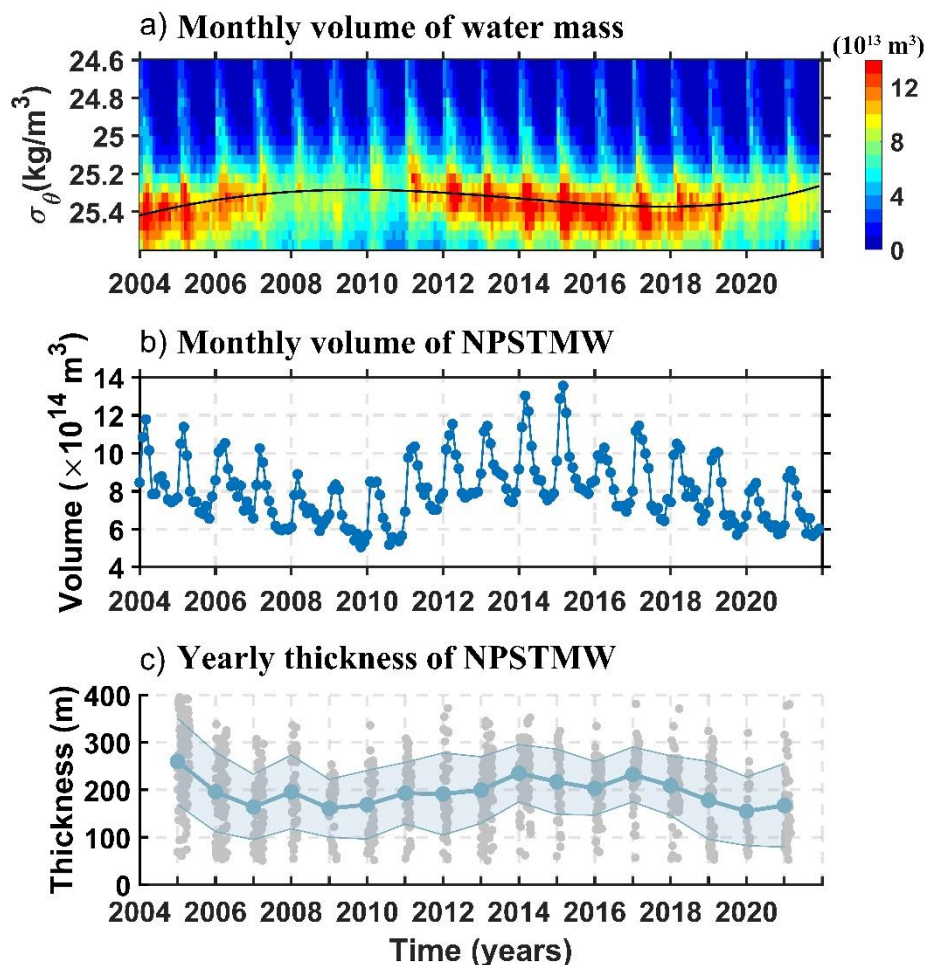
Figure 4: (a) Monthly averaged water mass volume (10^{13} m^3) estimated from the RG dataset for the years 2004-2021, in the
potential density range σ_θ =24.6-25.6 kg m^{-3} (color, right bar) with PV<2×10^{-10} m^{-1} s^{-1}. The black line is cubic fit to monthly
volume maximum. (b) Monthly time series of volume of NPSTMW with σ_θ =25.0-25.5 kg m^{-3} obtained from the RG dataset. Both
estimates are obtained over the analysis region 20°N-40°N, 125°E-180°, east of Japan. (c) The time series of NPSTMW thickness
during the period of yearly maximum thickness (April-May). Gray circles represent values observed from individual Argo profiles
in the RG region. The circles-line represents mean values and the shading around each line shows the standard deviation.

3.2 Decrease in the NPSTMW surface formation

Surface water mass transformation and formation rates have been introduced in section 2.3. Inputs to this analysis are
monthly estimates of air-sea buoyancy flux and of surface density in winter. First, maps of annually averaged surface
formation rate in the NPSTMW density range during 2012-2015 and 2018-2021 when the KE is similarly in a stable state are
shown in Figure 5. The averaged areas of the NPSTMW outcrop window of 2.67×10^{12} m^2 during 2018-2021 do not shrink
remarkably relative to 3.08×10^{12} m^2 during 2012-2015 (Figure 6). Because the less changes in the position of KE jet when

KE is in a stable state period (Suga and Hanawa, 1990), not as the case in 2006-2009 when the smallest NPSTMW outcropping window was attributed to the spatially convoluted path of the KE in the unstable state (Cerovečki and Giglio, 2016). In a stable KE period of 2012-2015, the strong surface formation tends to happen in the upstream of KE (141°E-153°E). However, the averaged surface formation in the upstream of KE has declined in recent stable KE period (Figure 5).

205 The mean heat flux loss in the outcrop window during 2018-2021 has decreased by 14% relative to 2012-2015 (Figure 6). Equation (4) shows that the water mass transformation will be weak owing to the less surface ocean buoyancy loss over the reduced outcropping window. It is the decline of surface buoyancy flux loss and outcrop window in the wintertime of 2018-2021 (Figure 6) that further inhabits the ocean surface water mass formation in the NPSTMW density range.
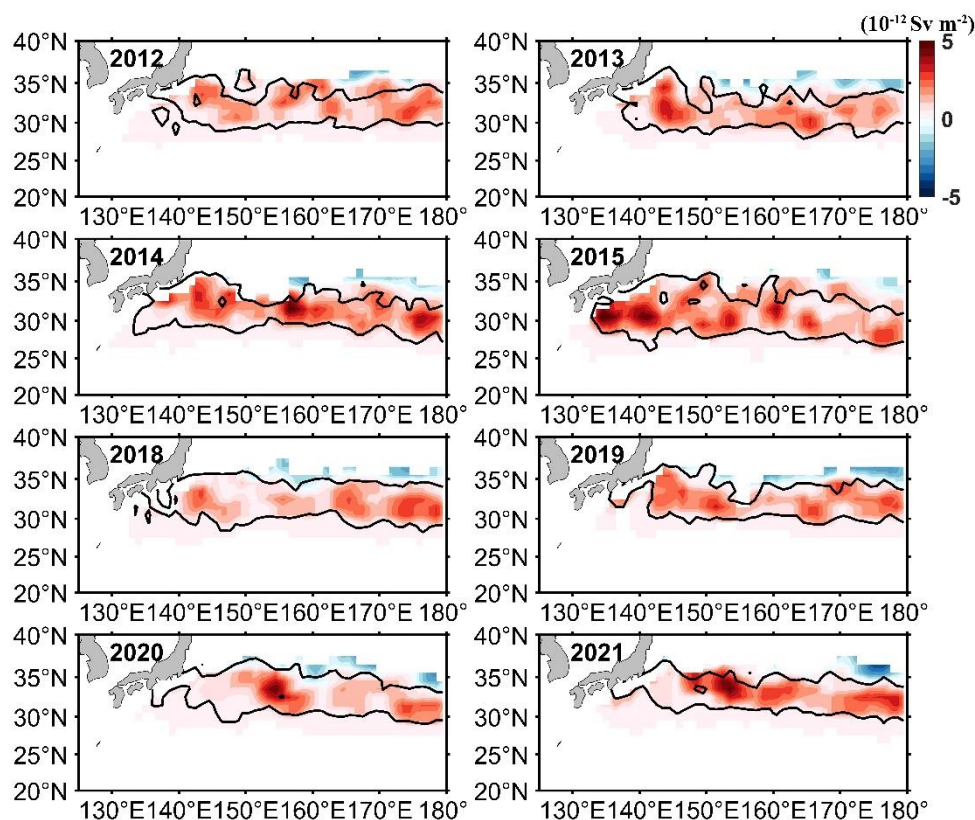
210 **Figure 5: Maps of annually averaged surface formation rate per unit area (10^{-12} Sv m^{-2}) in the NPSTMW density range. The solid lines bound the σ_θ =25.0-25.5 kg m^{-3} outcrop region time averaged from January to March.**
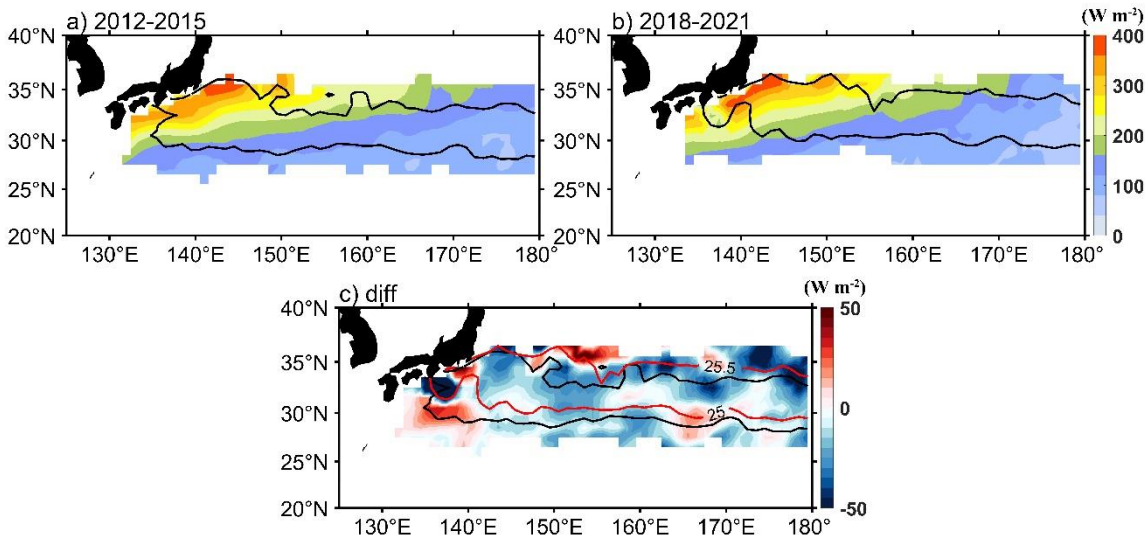
Figure 6: The averaged NHF loss (W m^{-2}) for years (a) 2012-2015 and (b) 2018-2021 in wintertime (January-March). The solid lines bound the σ_θ=25.0-25.5 kg m^{-3} outcrop region time averaged from January to March. (c) The difference (the values of 2018-2021 minus that of 2012-2015) from ERA5 in the outcrop region between the ensembled wintertime NHF (W m^{-2}) in the 2018-2021 and that in 2012-2015 (positive values represent the larger ocean heat loss). The outcropping lines of σ_θ=25.0 kg m^{-3} (the southernmost one) and 25.5 kg m^{-3} (the northernmost one) are superimposed in the black solid (2012-2015) and red solid contours (2018-2021).

Furthermore, in each of years considered, the annually averaged surface transformation and formation rates binned into the potential density at σ_θ=0.1 kg m^{-3} are shown in Figure 7. Figure 7 (a) and (c) show the annually averaged surface transformation rate in 2012-2015 and 2018-2021, respectively. Over the time period 2018-2021, transformation rates in the lighter NPSTMW density range (approximately σ_θ<25.2 kg m^{-3}) compared to the time period 2012-2015 were greatly reduced. Decreased transformation as well reflects decrease in surface buoyancy loss in 2018-2021. In addition, the annually averaged surface formation rates over the time period 2018-2021 have a pronounced peak in the lighter NPSTMW density range (approximately σ_θ<25.2 kg m^{-3}) (Figure 6d). Decreased formation in denser NPSTMW density range (approximately σ_θ>25.2 kg m^{-3}), but larger formation of lighter density range in NPSTMW further reflects the decrease of the NPSTMW density in 2018-2021. The recent attenuated formation of the NPSTMW in denser density (approximately σ_θ>25.2 kg m^{-3}) further demonstrates that this is associated with the decreasing surface buoyancy loss (Figure 6), as indicated by Eq. (6).
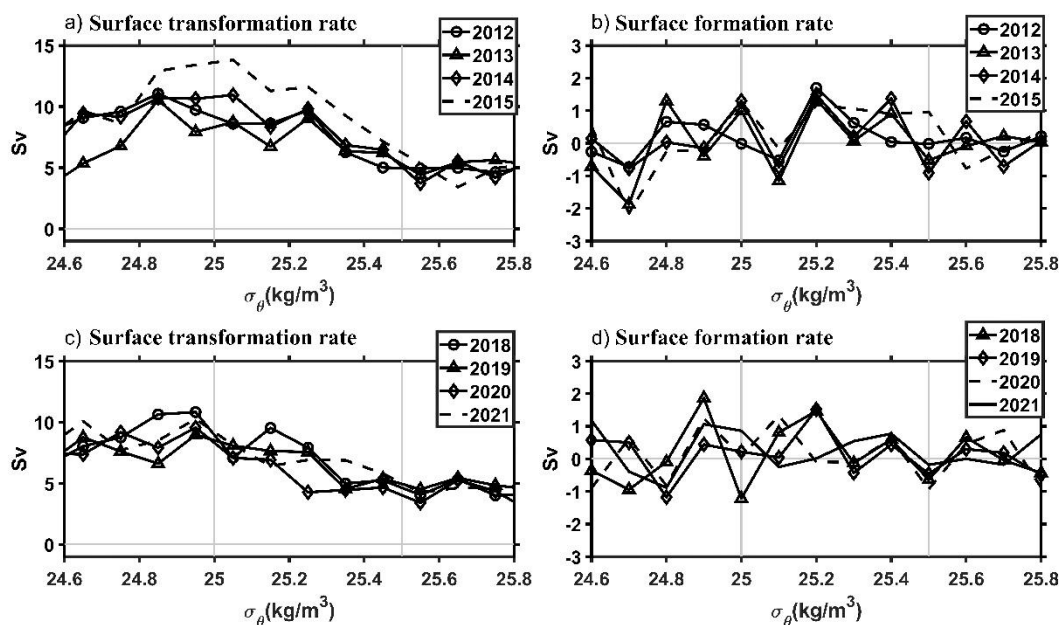
Figure 7: Annually averaged (a) and (c) surface transformation rate and (b), (d) formation rate obtained from ERA5 air-sea buoyancy flux using the Walin (1982) framework within the wintertime isopycnal outcrop region.

3.3 Decrease in subduction rate and NPSTMW subduction variability

After formation of the low-PV water within the NPSTMW density range in winter, the newly wintertime low-PV water mass is subsequently subducted into the ocean interior forming NPSTMW in late winter and early spring. Figure 8 compares the patterns of subduction rate between 2012-2015 and 2018-2021. The large subduction of NPSTMW usually occurs in the RG region south of KE, as depicted in Figure 8a. However, the total subduction rate of 2018-2021 reduced significantly in the RG region, even dropped by reaching 90 m year^{-1} (Figure 8c). Here, the subduction rate changes in 2018-2021 are predominantly caused by the temporal induction and lateral induction terms, while the vertical pumping term is negligible (Figure 8d-8f). The evident negative anomalies of temporal induction and lateral induction can be attributed to the anomalously shallow MLD located at the south of KE (Figure 9a). The wintertime (February-March) MLD in the RG region from individual Argo float profiles (Figure 9b) presents the same way like Figure 9a: the MLD in 2018-2021 is anomalously shallower than 2012-2015 by approximately 50 m on average in a stable KE period. Additionally, it is interesting to note that the mean outcropping isopycnals in NPSTMW densely range has a clear northward movement in 2018-2021, comparing to that located in 2012-2015.
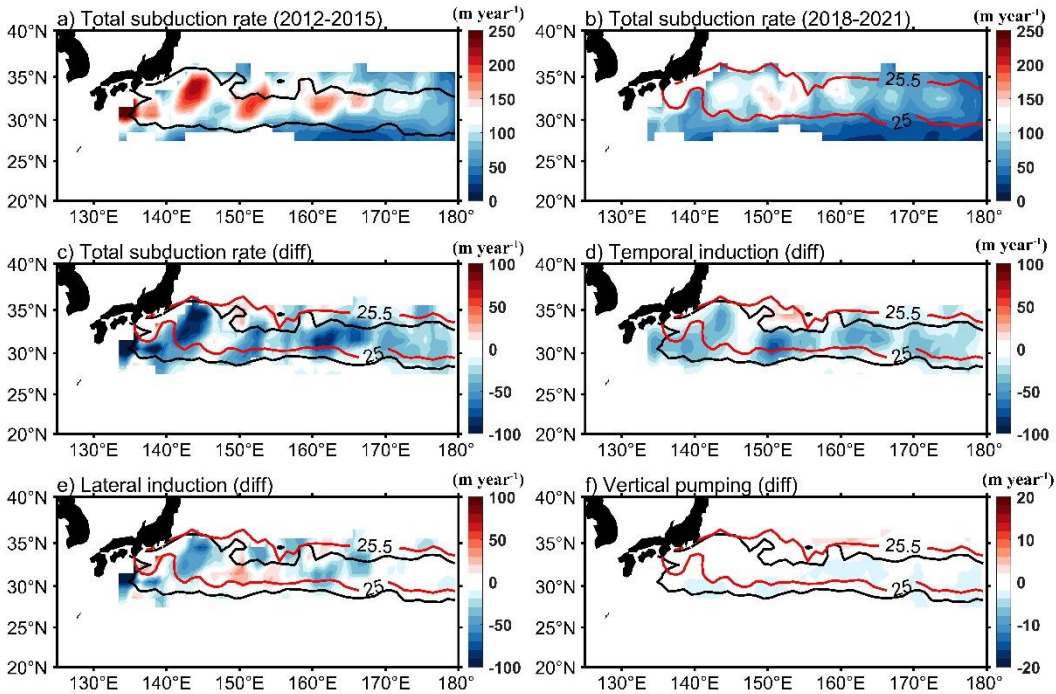
Figure 8: (a) the total subduction rate of 2012-2015 (b) the total subduction rate of 2018-2021 (c) the difference (the values of 2018-2021 minus that of 2012-2015) between the ensembled subduction rate (m year⁻¹) and three components responsible for the subduction rate change in the outcrop region: (d) temporal induction ($-\dfrac{1}{T_0}\int_{T_s^{ef}}^{T_e^{ef}}\dfrac{\partial \bar{h}}{\partial t}dt$), (e) lateral induction ($-\dfrac{1}{T_0}\int_{T_s^{ef}}^{T_e^{ef}}\left(\bar{\mathbf{u}}\cdot\nabla\bar{h}\right)dt$), and (f) vertical pumping ($-\dfrac{1}{T_0}\int_{T_s^{ef}}^{T_e^{ef}}\bar{w}dt$). Here, *t* is time, T_0 is one year and T_s^{ef} and T_e^{ef} are the times when effective subduction starts and ends, respectively (i.e., from February to April) (Marshall et al., 1993). The outcropping lines of σ_θ =25.0 kg m⁻³ (the southernmost one) and 25.5 kg m⁻³ (the northernmost one) are superimposed in the black solid (2012-2015) and red solid contours (2018-2021). The results obtained from RGA/ERA5 datasets with imposing the PV constraint (<2×10⁻¹⁰ m⁻¹ s⁻¹ of Eq. (2)).
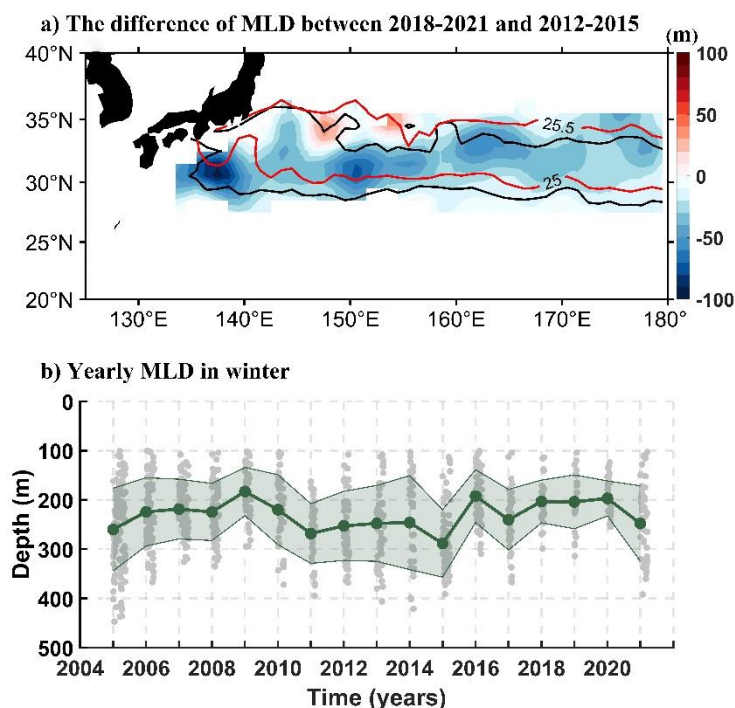
Figure 9: The difference (the values of 2018-2021 minus that of 2012-2015) in the outcrop region between the ensembled
wintertime MLD (m) in the 2018-2021 and that in 2012-2015. The outcropping lines of σ_θ =25.0 kg m^{-3} (the southernmost one)
and 25.5 kg m^{-3} (the northernmost one) are superimposed in the black solid (2012-2015) and red solid contours (2018-2021). (b)
The time series of MLD in February-March in the RG region south of KE (30°N-34°N, 141°E-153°E). Gray circles represent
values observed from individual Argo profiles in the RG region. The circles-line represents mean values and the shading around
each line shows the standard deviation.

Due to the anomalously shallow wintertime MLD, the subduction rate that occurred in the NPSTMW formation region
dropped largely in 2018-2021. Consequently, the subduction volume of NPSTMW drop from 5.60×10^{14} m^3 in 2015 to 2.99
$\times 10^{14}$ m^3 in 2021 (Figure 10). Especially in 2018-2021, the total subduction volume of NPSTMW in the ventilation region
has declined by 41% on average. In 2018-2021, the decrease of NPSTMW subduction in the south of KE region is mostly
attributed to the lateral induction and temporal induction volume. What is more, the interannual variability of NPSTMW
subduction volume in 2018-2021 mostly depends on wintertime MLD change (Figure 9).
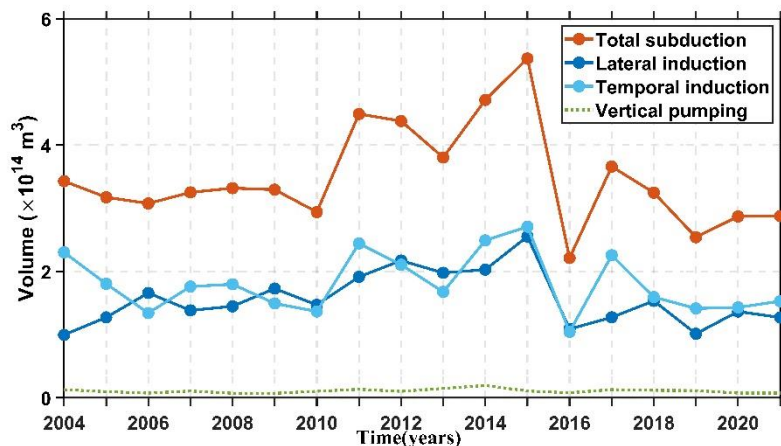
Figure 10: Annually-averaged total subduction volume and its three components: temporal induction volume ($-\int_{T_s^{ef}}^{T_e^{ef}}\left[\sum\left(\frac{\partial\overline{h}}{\partial t}\right)\Delta A\right]dt$)

from the monthly mean RG dataset, lateral induction volume ($-\int_{T_s^{ef}}^{T_e^{ef}}\left[\sum\left(\overline{\mathbf{u}}\cdot\nabla\overline{h}\right)\Delta A\right]dt$) from the monthly mean RG dataset, and

vertical pumping ($-\int_{T_s^{ef}}^{T_e^{ef}}\left[\sum\left(\overline{w}\right)\Delta A\right]dt$) from the monthly mean ERA5 data and annually-averaged volume of NPSTMW over the

270 Northwestern Pacific Ocean (125°E-180°, 20°N-40°N) from the monthly mean RG dataset for 2004-2021. The results obtained with imposing the PV constraint ($<2\times10^{-10}$ m^{-1} s^{-1} of Eq. (2)).

3.4 Local and distant effects on NPSTMW formation and subduction

Except for the KE dynamic state change, the NPSTMW interannual variability has been closely tied to the basin-wide changes of both atmospheric forcing and oceanic precondition associated with the PDO, both in observations (Qiu and Chen,

275 2006) and numerical model results (Davis et al., 2011). The NPSTMW volume variations in 2006-2009 (2012-2015) (Figure 2b) are closely controlled by the MTD because the PDO-related stronger (weaker) background stratification propagated from the central North Pacific (Figure 11). Meanwhile, Figure 11 also shows the distant effects of MTD (i.e., background stratification) change on NPSTMW formation in the western North Pacific with some time lag (about 3-4 years). However, since 2018, the PDO has transitioned from a positive to negative phase (Figure 11a), with the concomitant positive SSH

280 anomaly and deepened MTD (Figure 11b and 11c). The positive MTD anomaly which weakens the background stratification should have facilitated the development of wintertime MLD and NPSTMW formation, as suggested as that in 2012-2015. On the contrary, the MLD and the subduction of NPSTMW do not have such sufficient developments in the late winter of 2018-2021 (Figure 9 & 10). Additionally, the recently anomalous NPSTMW decline also follows the PDO phase shift. Thus, the subtle time lag between PDO shift and NPSTMW may have more important implications to investigate next.
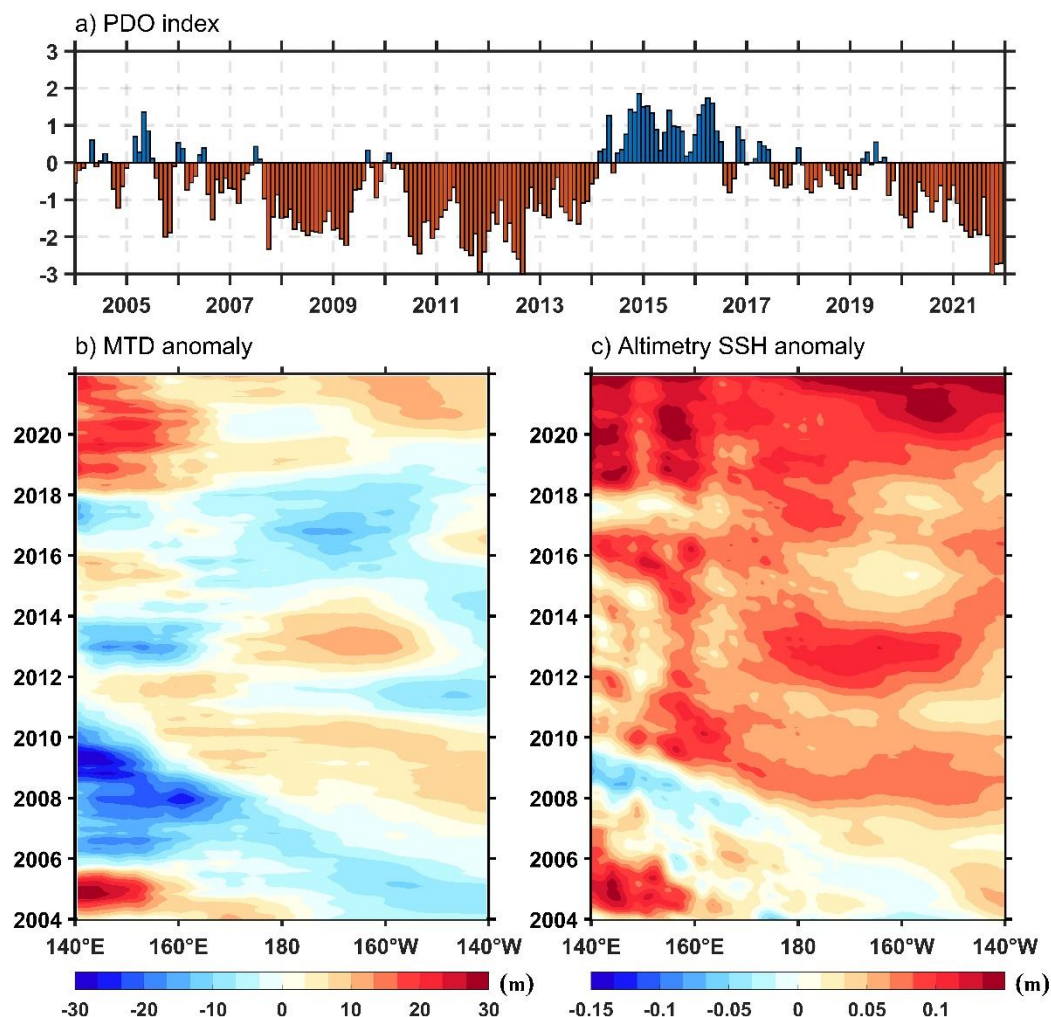
Figure 11: (a) Monthly values of the PDO index (Mantua, 1999). (b) Longitude–time diagram of MTD anomaly (m) (MTD anomaly obtained from RG dataset) averaged for a zonal band of 30°N-34°N. Positive (negative) values represent deep (shallow) anomalies. (c) as in (b), but for the satellites-altimetry SSH anomaly (m). (SSH anomaly provided by CMEMS has a one-day temporal resolution and a 1/4° spatial resolution from January 1993 to December 2021).

Here, the dynamics and thermodynamics of anomalous NPSTMW variability in 2018-2021, particularly in recently persisting stable KE state, are sought by examining wind stress and surface heat flux associated with an instantaneous response to events in the central Pacific (i.e., the PDO phase shift). When the PDO phase turned from a positive into negative phase in 2018-2021, the AL shifted northward (Figure 12b and 12c) and negative wind stress curl anomalies were generated in the central Pacific (Figure 12a). The basin-scale atmospheric forcing impacts a remarkable influence on the subtropical gyre region (Figure 12). It appears that the AL northward shift and subsequent changes of the intensity of westerlies corresponds to the reduced NPSTMW formation in 2018-2021 compared with that in 2012-2015. The weaker westerlies in NPSTMW formation area lead to less Ekman transport of the cold water from the north. The averaged

magnitude of southward meridional Ekman transport ($T_y = -\tau_x/(\rho f)$) occurred in the NPSTMW formation region has

declined by 31% during 2018-2021 relative to 2012-2015.
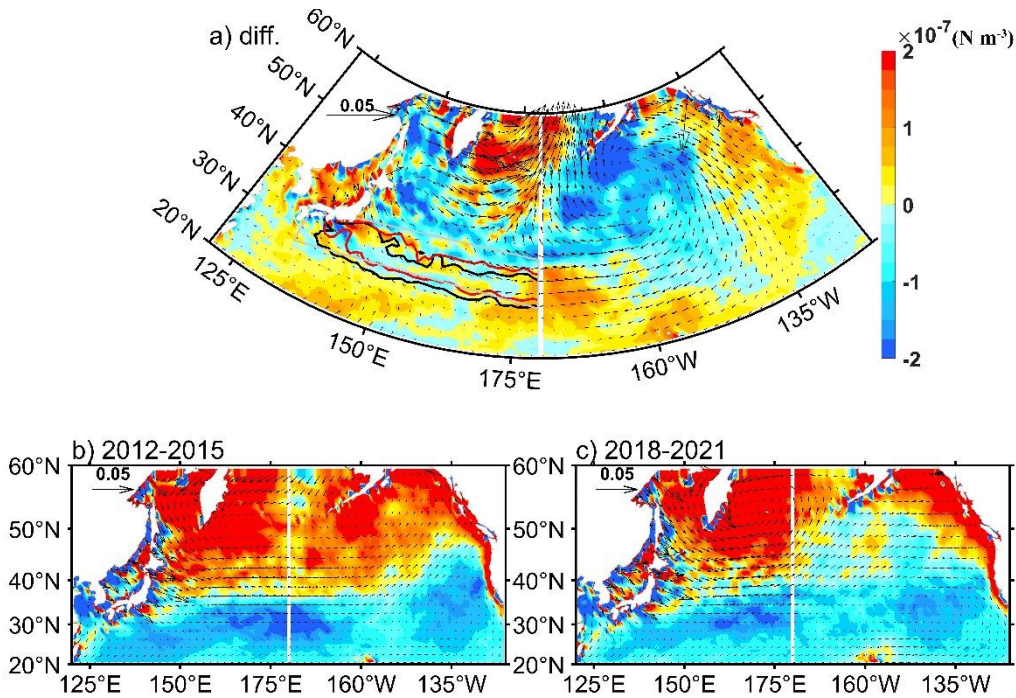
300

Figure 12: The ensembled wintertime (January-March) surface wind stress (vectors; N m^{-2}) and wind stress curl (color shading; N m^{-3}) in North Pacific Ocean from ERA5 in (b) 2012-2015 and (c) 2018-2021; (a) the difference between (c) and (b) (i.e., (c) minus (b)). The outcropping lines of σ_θ =25.0 kg m^{-3} (the southernmost one) and 25.5 kg m^{-3} (the northernmost one) are superimposed in the black solid (2012-2015) and red solid contours (2018-2021). The gray box in the figures indicates the area of NPSTMW formation and subduction (132°E-180°, 28°N-36°N).

305

First, the recently observed NPSTMW volume loss appears closely related to the intensity of the prevailing westerlies during the period of PDO phase shift. During 2018-2021, the westerlies occur between 30°N and 50°N, with the AL residing to the north over the subpolar gyre (Figure 12c). The intensity of the westerlies weakens in the western part of the basin. The northward shift of the westerlies causes a weaker wind to its south better approximately 30°N and 40°N (Figure 12a, i.e., the

310 area of NPSTMW formation and subduction). Consequently in 2018-2021, a persisting weakening of the intensity of wintertime surface wind stress is leaded over the outcropping window (Figure 12a). During the cold season, weakening of the overlying wind stress can subsequently prohibit the local heat loss in the NPSTMW formation region (Bond and Cronin, 2008). Meanwhile, the monthly time-depth section of temperature, stratification anomalies and MLD averaged within the ventilation region is indicated in Figure 13. The intensified preconditioning of near surface stratification (<150 m) since

315 2018 has increased due to the remarkable near sea surface warming. This may further inhibit the necessary wintertime

convection (i.e., the origin of the deep MLD in winter) essential for new NPSTMW formation in the following winter (Tomita et al., 2010).
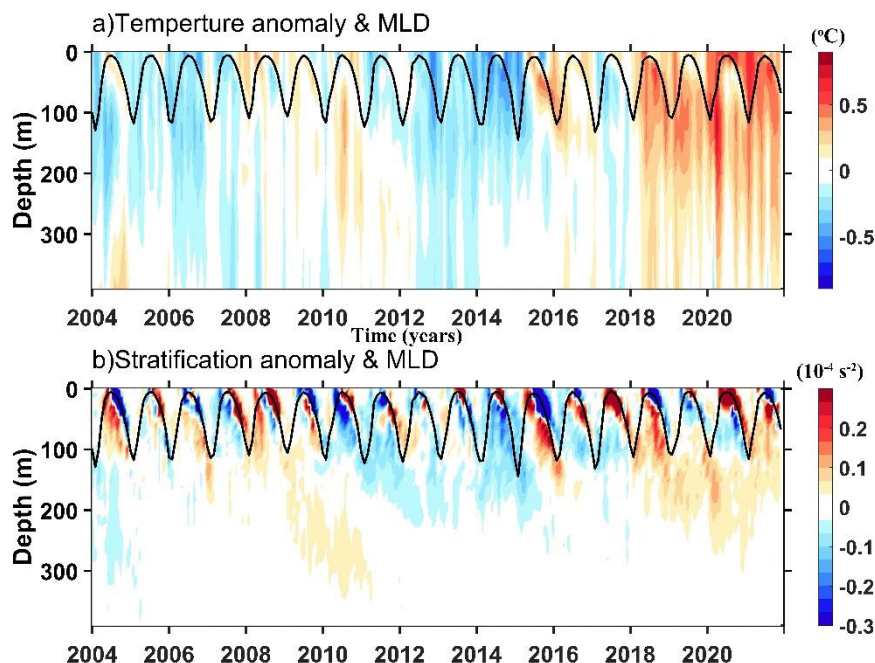
Figure 13: Monthly time series of (a) temperature anomaly (ºC), (b) stratification anomaly (10⁻⁴ s⁻²) and MLD (black lines) obtained from RG dataset averaged over the NPSTMW formation region.

Indeed, as a result of the poleward shift of the westerlies, local easterly wind anomalies are shown over the NPSTMW formation region during the winter of 2018-2021 (Figure 12a), which cause the northward Ekman transport. The anomalous northward Ekman advection of shallow ML with lighter densities would cause the northward migration of the NPSTMW outcropping lines (Figure 14c). Thus, the suppressed local heat loss and northward migration of lighter densities from south are coherent with the appearance of wintertime surface lighter density water mass (Figure 14).
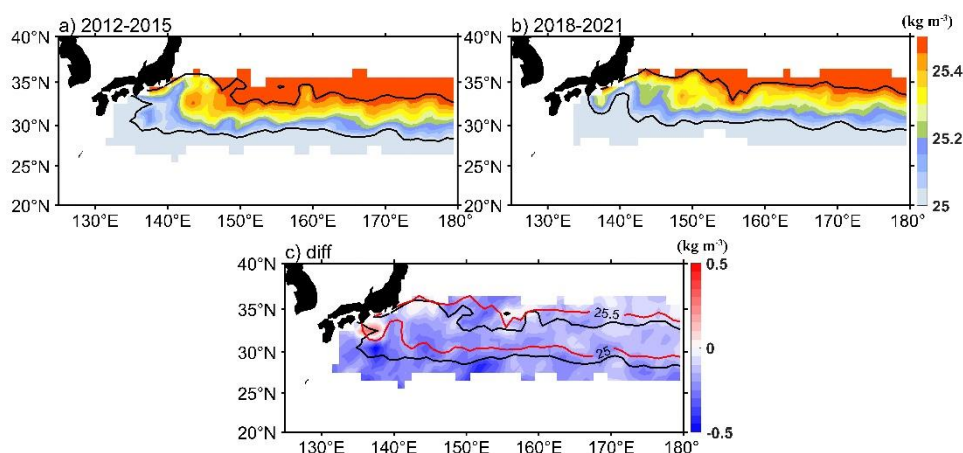
Figure 14: The averaged surface potential density (kg m⁻³) for years (a) 2012-2015 and (b) 2018-2021 in wintertime (January-March). The solid lines bound the σ_θ =25.0-25.5 kg m⁻³ outcrop region time averaged from January to March. (c) anomalies of surface potential density for years 2018-2021, as a deviation from the wintertime time mean (over 2012-2015) of surface potential density, in kg m⁻³. The outcropping lines of σ_θ =25.0 kg m⁻³ and 25.5 kg m⁻³ are superimposed in the black solid (2012-2015) and red solid contours (2018-2021).

4 Summary and Discussion

Though the KE jet is in a persistent stable state during a recent time of 2018-2021 which is somewhat analogous to the stable KE state in 2012-2015, the anomalous decrease of the NPSTMW volume and density in 2018-2021 have been observed from the Argo observation data. This is particularly pronounced in the subtropical RG region during winter and is most evident near the KE bounded by 30°N-34°N, 141°E-153°E. The mean NPSTMW volume drop by ~21% during 2018-2021 relative to 2012-2015 in the whole NPSTMW formation region. The density decrease is presented as the loss of NPSTMW volume in denser density range (approximately σ_θ >25.2 kg m⁻³) since 2018, but the increase of NPSTMW volume in lighter density range (approximately σ_θ <25.2 kg m⁻³).

Although the KE is in a persisting stable state of 2018-2021, the NPSTMW volume loss is found in an analysis period when the PDO changes from its positive phase to a negative phase. The correlation between NPSTMW volume variability and the PDO index suggests that the NPSTMW variability is link to the modulation of the basin-scale atmospheric forcing. We can be enlightened how these mechanisms may play a role in interannual NPSTMW variability through an identification of analogous cases in the precedent studies. Previous studies have linked the KE dynamic state changes to the basin-scale wind pattern. However, the distant effect is the first baroclinic Rossby wave as the primary message of wind variability from the central Pacific to the NPTMW formation region over a time lag of ~4 years (Sugimoto & Hanawa, 2010). The variabilities of MTD anomalies and KE state due to PDO (a ~4-yr lag) are corresponding to the propagation speed of the first baroclinic Rossby wave. The results presented in this study shows that there is no significant time lag of the distant effect between NPSTMW variability and the change of basin-scale wind stress pattern (i.e., the PDO phase shift). This suggests that different mechanisms account for the NPSTMW formation in 2018-2021. The interannual signal is evident in the changes of NPSTMW volume, density and outcropping isopycnals moving, with this signal determined by the yearly difference in NPSTMW formation and subduction. The distinct interannual signal of NPSTMW in 2018-2021 is correlated well with PDO changes from its positive phase to a negative phase in recent years. It is supported by studies of the formation and subduction rate in the northwestern Pacific. In 2018-2021, the surface formation rate intensely declines in the upstream of KE (141°E-153°E). Meanwhile, the formation rate in denser NPSTMW density range (approximately σ_θ >25.2 kg m⁻³) decreases greatly. The total subduction volume of NPSTMW in the ventilation region subsequently has declined by 41% on average. Furthermore, the interannual variability of NPSTMW subduction is directly linked to the ML change. Such insufficient development of wintertime ML in the ventilation region of northwestern Pacific and decline of NPSTMW formation are

associated with the less heat loss and large-scale wind stress change in 2018-2021. This result is in agreement with the

360   negative phase of the PDO shift studied here.

Although occurred locally, interannual variability of NPSTMW is intensely associated with the shift of basin-scale wind pattern. Based on this work, the dynamic impact of large-scale wind modification on the recent NPSTMW changes has been further examined, which resembles the theoretical framework in Davis et al. (2010). A scenario for these correlations of the physical causality (i.e., linear dependency) are that (1) The northward shift of the westerlies when the PDO shift from a

365   positive to a negative phase in 2018-2021 produces a weaker wintertime wind stress over the NPSTMW formation region, resulting in less heat loss to the atmosphere and shallower wintertime ML. Furthermore, the annual subduction dominated by lateral induction and temporal induction subsequently decline largely associated with wintertime ML change. (2) As a result of the poleward shift of the westerlies, easterly wind anomalies in the NPSTMW formation region cause the northward Ekman transport of the shallower ML with lighter densities from south. Additionally, the strengthening of KE jet in a

370   persisting stable KE period that favors a northward shift of the KE jet may cause warming of the sea surface temperature in the KE region (Qiu, 2000). The significantly intensified preconditioning of near surface stratification (<150 m depth) associated with near surface warming is also a relevant factor. They restrain wintertime convection and deepening of the ML, resulting in reduced transformation and formation of water in the NPSTMW density range. The decrease of surface density further decreases the density of the NPSTMW low PV pool.

375   The salient contribution of this study is that it reveals the anomalously decreasing NPSTMW in 2018-2021 is strongly associated with a response to a PDO phase shift event. We believe the that results of this study will be a step toward the deep understanding of the relationship between NPSTMW interannual variations and modulation of basin-scale wind pattern in recent years. Owing to the NPSTMW wide range of influence, the present study may have broad implications for climate change and biogeochemical cycles (Holbrook et al., 2019; Kuroda and Setou, 2021; Tak et al., 2021).

380   **Data availability**

The gridded Argo product was obtained from Roemmich-Gilson Argo Climatology (https://sio-argo.ucsd.edu/RG_Climatology.html). The monthly mean net heat flux and wind stress products are obtained from ECMWF-ERA5 (https://doi.org/10.24381/cds.f17050d7). The sea surface height anomaly is provided by CMEMS (https://doi.org/10.48670/moi-00148, https://doi.org/10.48670/moi-00149).

385   **Author contributions**

JS and CL planned the study. JS, CL and YZG designed the analysis framework. JS processed data, conducted the analysis, and wrote the paper. ZN collected the data. CL, YZG, FGZ and PLL contributed with the analysis performance and

interpretation of the results. JS and CL revised and edited the final version of the paper.

Competing interests

The contact author has declared that none of the authors has any competing interests.

Disclaimer

Publisher's note: Copernicus Publications remains neutral with regard to jurisdictional claims in published maps and institutional affiliations.

Acknowledgments

The Argo Program is part of the Global Ocean Observing System. These data were collected and made freely available by the International Argo Program and the national programs that contribute to it (http://www.argo.ucsd.edu; http://argo.jcommops.org).

Financial support

The work was jointly supported by the National Natural Science Foundation of China (grant no. 42206003), the Scientific and technological projects of Zhoushan (2022C81010), the Major program of Pilot National Laboratory for Marine Science and Technology (Qingdao) (2022QNLM040004-3), the Finance science and technology project of hainan province (ZDKJ202019), and the National Science Foundation of China (grant no. 42176016).

References

Akima, H.: A new method of interpolation and smooth curve fitting based on local procedures, J. ACM JACM, 17, 589–602, 1970.

Bond, N. A. and Cronin, M. F.: Regional Weather Patterns during Anomalous Air–Sea Fluxes at the Kuroshio Extension Observatory (KEO)*, J. Clim., 21, 1680–1697, https://doi.org/10.1175/2007JCLI1797.1, 2008.

Cerovečki, I. and Giglio, D.: North Pacific Subtropical Mode Water Volume Decrease in 2006–09 Estimated from Argo Observations: Influence of Surface Formation and Basin-Scale Oceanic Variability, J. Clim., 29, 2177–2199, https://doi.org/10.1175/JCLI-D-15-0179.1, 2016.

Cerovečki, I. and Marshall, J.: Eddy modulation of air–sea interaction and convection, J. Phys. Oceanogr., 38, 65–83, 2008.

Cerovečki, I., Hendershott, M. C., and Yulaeva, E.: Strong North Pacific Subtropical Mode Water Volume and Density Decrease in Year 1999, J. Geophys. Res. Oceans, 124, 6617–6631, https://doi.org/10.1029/2019JC014956, 2019.

415 Cushman-Roisin, B.: Subduction. Dynamics of the Oceanic Surface Mixed Layer: Proc.'Aha Huliko'a Hawaiian Winter Workshop, Honol. HI Univ. Hawaii Manoa, 181, 196, 1987.

Davis, X. J., Rothstein, L. M., Dewar, W. K., and Menemenlis, D.: Numerical Investigations of Seasonal and Interannual Variability of North Pacific Subtropical Mode Water and Its Implications for Pacific Climate Variability, J. Clim., 24, 2648–2665, https://doi.org/10.1175/2010JCLI3435.1, 2011.

420 Garrett, C. and Tandon, A.: The effects on water mass formation of surface mixed layer timedependence and entrainment fluxes, Deep Sea Res. Part Oceanogr. Res. Pap., 44, 1991–2006, 1997.

Guo, Y., Lin, X., Wei, M., Liu, C., and Men, G.: Decadal Variability of North Pacific Eastern Subtropical Mode Water, J. Geophys. Res. Oceans, 123, 6189–6206, https://doi.org/10.1029/2018JC013890, 2018.

Hanawa, K. and Kamada, J.: Variability of core layer temperature (CLT) of the North Pacific Subtropical Mode Water,
425 Geophys. Res. Lett., 28, 2229–2232, https://doi.org/10.1029/2000GL011716, 2001.

Hersbach, H., Bell, B., Berrisford, P., Biavati, G., Horányi, A., Muñoz Sabater, J., Nicolas, J., Peubey, C., Radu, R., Rozum, I., and others: ERA5 monthly averaged data on single levels from 1979 to present, Copernic. Clim. Change Serv. C3S Clim. Data Store CDS, 10, 252–266, 2019.

Holbrook, N. J., Scannell, H. A., Sen Gupta, A., Benthuysen, J. A., Feng, M., Oliver, E. C. J., Alexander, L. V., Burrows, M.
430 T., Donat, M. G., Hobday, A. J., Moore, P. J., Perkins-Kirkpatrick, S. E., Smale, D. A., Straub, S. C., and Wernberg, T.: A global assessment of marine heatwaves and their drivers, Nat. Commun., 10, 2624, https://doi.org/10.1038/s41467-019-10206-z, 2019.

Kuroda, H. and Setou, T.: Extensive Marine Heatwaves at the Sea Surface in the Northwestern Pacific Ocean in Summer 2021, Remote Sens., 13, 3989, https://doi.org/10.3390/rs13193989, 2021.

435 Levitus, S.: Climatological atlas of the world ocean, US Department of Commerce, National Oceanic and Atmospheric Administration, 1982.

Liu, C., Xie, S., Li, P., Xu, L., and Gao, W.: Climatology and decadal variations in multicore structure of the N orth P acific subtropical mode water, J. Geophys. Res. Oceans, 122, 7506–7520, https://doi.org/10.1002/2017JC013071, 2017.

Mantua, N.: The Pacific Decadal Oscillation: a brief overview for non-specialists, Encycl. Environ. Change, 1999.

440 Marshall, D.: Subduction of water masses in an eddying ocean, J. Mar. Res., 55, 201–222, https://doi.org/10.1357/0022240973224373, 1997.

Marshall, J., Jamous, D., and Nilsson, J.: Reconciling thermodynamic and dynamic methods of computation of water-mass transformation rates, Deep Sea Res. Part Oceanogr. Res. Pap., 46, 545–572, https://doi.org/10.1016/S0967-0637(98)00082-X, 1999.

445 Masuzawa, J.: Subtropical mode water, in: Deep sea research and oceanographic abstracts, 463–472, 1969.

Newman, M., Alexander, M. A., Ault, T. R., Cobb, K. M., Deser, C., Di Lorenzo, E., Mantua, N. J., Miller, A. J., Minobe, S., Nakamura, H., Schneider, N., Vimont, D. J., Phillips, A. S., Scott, J. D., and Smith, C. A.: The Pacific Decadal Oscillation, Revisited, J. Clim., 29, 4399–4427, https://doi.org/10.1175/JCLI-D-15-0508.1, 2016.

Oka, E. and Qiu, B.: Progress of North Pacific mode water research in the past decade, J. Oceanogr., 68, 5–20, https://doi.org/10.1007/s10872-011-0032-5, 2012.

Oka, E., Talley, L. D., and Suga, T.: Temporal variability of winter mixed layer in the mid-to high-latitude North Pacific, J. Oceanogr., 63, 293–307, https://doi.org/10.1007/s10872-007-0029-2, 2007.

Oka, E., Kouketsu, S., Toyama, K., Uehara, K., Kobayashi, T., Hosoda, S., and Suga, T.: Formation and Subduction of Central Mode Water Based on Profiling Float Data, 2003–08, J. Phys. Oceanogr., 41, 113–129, https://doi.org/10.1175/2010JPO4419.1, 2011.

Oka, E., Qiu, B., Takatani, Y., Enyo, K., Sasano, D., Kosugi, N., Ishii, M., Nakano, T., and Suga, T.: Decadal variability of Subtropical Mode Water subduction and its impact on biogeochemistry, J. Oceanogr., 71, 389–400, https://doi.org/10.1007/s10872-015-0300-x, 2015.

Oka, E., Yamada, K., Sasano, D., Enyo, K., Nakano, T., and Ishii, M.: Remotely Forced Decadal Physical and Biogeochemical Variability of North Pacific Subtropical Mode Water Over the Last 40 Years, Geophys. Res. Lett., 46, 1555–1561, https://doi.org/10.1029/2018GL081330, 2019.

Oka, E., Nishikawa, H., Sugimoto, S., Qiu, B., and Schneider, N.: Subtropical Mode Water in a recent persisting Kuroshio large-meander period: part I—formation and advection over the entire distribution region, J. Oceanogr., 77, 781–795, 2021.

Qiu, B.: Interannual variability of the Kuroshio Extension system and its impact on the wintertime SST field, J. Phys. Oceanogr., 30, 1486–1502, 2000.

Qiu, B.: Kuroshio Extension Variability and Forcing of the Pacific Decadal Oscillations: Responses and Potential Feedback, J. Phys. Oceanogr., 33, 2003.

Qiu, B. and Chen, S.: Variability of the Kuroshio Extension Jet, Recirculation Gyre, and Mesoscale Eddies on Decadal Time Scales, J. Phys. Oceanogr., 35, 2090–2103, https://doi.org/10.1175/JPO2807.1, 2005.

Qiu, B. and Chen, S.: Decadal Variability in the Formation of the North Pacific Subtropical Mode Water: Oceanic versus Atmospheric Control, J. Phys. Oceanogr., 36, 1365–1380, https://doi.org/10.1175/JPO2918.1, 2006.

Qiu, B. and Chen, S.: Revisit of the occurrence of the Kuroshio large meander South of Japan, J. Phys. Oceanogr., 51, 3679–3694, 2021.

Qiu, B., Hacker, P., Chen, S., Donohue, K. A., Watts, D. R., Mitsudera, H., Hogg, N. G., and Jayne, S. R.: Observations of the Subtropical Mode Water Evolution from the Kuroshio Extension System Study, J. Phys. Oceanogr., 36, 457–473, https://doi.org/10.1175/JPO2849.1, 2006.

Qiu, B., Chen, S., and Hacker, P.: Effect of Mesoscale Eddies on Subtropical Mode Water Variability from the Kuroshio Extension System Study (KESS), J. Phys. Oceanogr., 37, 982–1000, https://doi.org/10.1175/JPO3097.1, 2007.

480   Rainville, L., Jayne, S. R., McClean, J. L., and Maltrud, M. E.: Formation of Subtropical Mode Water in a high-resolution ocean simulation of the Kuroshio Extension region, Ocean Model., 17, 338–356, https://doi.org/10.1016/j.ocemod.2007.03.002, 2007.

Roemmich, D. and Gilson, J.: The 2004–2008 mean and annual cycle of temperature, salinity, and steric height in the global ocean from the Argo Program, Prog. Oceanogr., 82, 81–100, 2009.

485   Sasaki, Y. N. and Minobe, S.: Climatological mean features and interannual to decadal variability of ring formations in the Kuroshio Extension region, J. Oceanogr., 71, 499–509, https://doi.org/10.1007/s10872-014-0270-4, 2015.

Small, R. J., Bryan, F. O., and Bishop, S. P.: Surface Water Mass Transformation in the Southern Ocean: The Role of Eddies Revisited, J. Phys. Oceanogr., 52, 789–804, https://doi.org/10.1175/JPO-D-21-0087.1, 2022.

Suga, T. and Hanawa, K.: The mixed-layer climatology in the northwestern part of the North Pacific subtropical gyre and the
490   formation area of Subtropical Mode Water, J. Mar. Res., 48, 543–566, 1990.

Suga, T. and Hanawa, K.: Interannual variations of North Pacific subtropical mode water in the 137 E section, J. Phys. Oceanogr., 25, 1012–1017, 1995.

Suga, T., Hanawa, K., and Toba, Y.: Subtropical mode water in the 137 E section, J. Phys. Oceanogr., 19, 1605–1618, 1989.

Sugimoto, S. and Hanawa, K.: Impact of Aleutian Low activity on the STMW formation in the Kuroshio recirculation gyre
495   region: IMPACT OF AL ON THE STMW FORMATION, Geophys. Res. Lett., 37, n/a-n/a, https://doi.org/10.1029/2009GL041795, 2010.

Sugimoto, S. and Kako, S.: Decadal Variation in Winter Mixed Layer Depth South of the Kuroshio Extension and Its Influence on Winter Mixed Layer Temperature, J. Clim., 29, 1237–1252, https://doi.org/10.1175/JCLI-D-15-0206.1, 2016.

500   Tak, Y.-J., Song, H., and Cho, Y.-K.: Impact of the reemergence of North Pacific subtropical mode water on the multi-year modulation of marine heatwaves in the North Pacific Ocean during winter and early spring, Environ. Res. Lett., 16, 074036, https://doi.org/10.1088/1748-9326/ac0cad, 2021.

Taneda, T., Suga, T., and Hanawa, K.: Subtropical mode water variation in the northwestern part of the North Pacific subtropical gyre, J. Geophys. Res. Oceans, 105, 19591–19598, https://doi.org/10.1029/2000JC900073, 2000.

505   Tomita, H., Kako, S., Cronin, M. F., and Kubota, M.: Preconditioning of the wintertime mixed layer at the Kuroshio Extension Observatory, J. Geophys. Res. Oceans, 115, 2010JC006373, https://doi.org/10.1029/2010JC006373, 2010.

Toyama, K., Iwasaki, A., and Suga, T.: Interannual Variation of Annual Subduction Rate in the North Pacific Estimated from a Gridded Argo Product, J. Phys. Oceanogr., 45, 2276–2293, https://doi.org/10.1175/JPO-D-14-0223.1, 2015.

Uehara, H., Suga, T., Hanawa, K., and Shikama, N.: A role of eddies in formation and transport of North Pacific Subtropical
510   Mode Water: MESOSCALE EDDIES AND NPSTMW, Geophys. Res. Lett., 30, https://doi.org/10.1029/2003GL017542, 2003.

Usui, N.: Progress of Studies on Kuroshio Path Variations South of Japan in the Past Decade, in: Geophysical Monograph Series, edited by: Nagai, T., Saito, H., Suzuki, K., and Takahashi, M., Wiley, 147–161, https://doi.org/10.1002/9781119428428.ch9, 2019.

515 Walin, G.: On the relation between sea-surface heat flow and thermal circulation in the ocean, Tellus, 34, 187–195, https://doi.org/10.1111/j.2153-3490.1982.tb01806.x, 1982.

Williams, R. G.: The influence of air–sea interaction on the ventilated thermocline, J. Phys. Oceanogr., 19, 1255–1267, 1989.

Williams, R. G.: The role of the mixed layer in setting the potential vorticity of the main thermocline, J. Phys. Oceanogr., 21, 1803–1814, 1991.

520 Wu, B., Lin, X., and Yu, L.: North Pacific subtropical mode water is controlled by the Atlantic Multidecadal Variability, Nat. Clim. Change, 10, 238–243, https://doi.org/10.1038/s41558-020-0692-5, 2020.

Wu, B., Lin, X., and Yu, L.: Poleward Shift of the Kuroshio Extension Front and Its Impact on the North Pacific Subtropical Mode Water in the Recent Decades, J. Phys. Oceanogr., 51, 457–474, https://doi.org/10.1175/JPO-D-20-0088.1, 2021.